metals

MDPI

Article

A Partitioning Method for Friction Stir Welded Joint of AA2219 Based on Tensile Test

Guanglong Cao [1,2], Mingfa Ren [1,2], Yahui Zhang [2], Weibin Peng [3] and Tong Li [2,*]

1 State Key Laboratory of Structural Analysis for Industrial Equipment, Dalian University of Technology, Dalian 116024, China; cgllncn@mail.dlut.edu.cn (G.C.); renmf@dlut.edu.cn (M.R.)
2 Department of Engineering Mechanics, Dalian University of Technology, Dalian 116024, China; zhangyh@dlut.edu.cn
3 Beijing Institute Astronautical System Engineering, Beijing 100076, China; 18610933603@163.com
* Correspondence: tong@dlut.edu.cn; Tel.: +86-411-84706036

Received: 3 December 2019; Accepted: 27 December 2019; Published: 1 January 2020

check for updates

Abstract: The partition of aluminum alloy welded joint often depends on microscopic methods such as scanning electron microscopy before. This paper provides a novel partitioning method, which can obtain the material properties and partition results at the same time based on tensile test. The mechanical properties of every point on the whole welded joint are first obtained by the digital image correlation (DIC) method. Then, the mechanical property function of the weld joint along the weld center is established due to the changes of plastic property and strain hardening exponent at each point and the boundary between different areas is then determined. Metallographic detection technology and nano-mechanical testing techniques are employed to validate this partitioning scheme. The partition result of the strategy proposed in this paper is consistent with the partitioning result of the classical method. Compared to classical method, the proposed partitioning method is more practical and effective, as it can obtain mechanical properties and partition boundary through a single tensile test and reduce the cost of metallographic test.

Keywords: 2219 aluminum alloy; friction stir welded joint; partitioning; mechanical properties

1. Introduction

2219 aluminum alloy (AA2219) is widely used in aerospace engineering because of the outstanding formability, weldability, and high strength-to-weight ratio [1–3]. The major chemical composition in the heat-treatable AA2219 is copper except aluminum, which is required for precipitation strengthening. The strengthening of AA2219 can be further improved by refining the grain size to a few micrometers and lower in the alloy. This target can be achieved by friction stir processing, which is a solid-state processing technique developed from the principles of friction stir welding (FSW) and used for microstructural modification by grain refinement [4,5]. The stirring action of the rotating pin causes intense plastic deformation of the locally heated material. The combination of plastic deformation, mixing, and thermal exposure results in a modified microstructure in the weld zone (WZ), which is commonly characterized by fine and equiaxed grain structure with predominant high-angle boundaries. The modification is generally attributed to dynamic recrystallization and break-up of constituent particles [6]. Next to the WZ, a narrow transition region known as the thermo-mechanically affected zone (TMAZ) is formed, followed by the heat affected zone (HAZ), and finally the unaffected base metal (BM). In general, TMAZ is located on the dividing line between WZ and HAZ.

Due to the variation of mechanical properties at different positions in the welded joints, it is necessary to partition the welded joint to different regions while analyzing the mechanical performance of the welded joints. At present, a lot of achievements have been obtained by partitioning the welded joints to discuss their material properties [7–10]. There are two main methods to partition the aluminum alloy welded joints. One of them is to establish a relationship between hardness and material properties by means of hardness measurement, thereby dividing the welded joint into WZ, HAZ, and BM. He [11] sliced the aluminum alloy welded joint into a small tensile specimen, and measured the properties of a welded joint by indentation technique. J. Rojek [12] combined the tensile test, microhardness test, and obtained the stress-strain relationship of the welded joint by numerical inversion method, then the mechanical properties of each part of welded joints are given. Yazdipour [13] studied the friction stir welded joints by microstructure observation and hardness experiment, and summarized the mechanical properties of the BM, HAZ, TMAZ, and WZ.

Although these above methods can divide the aluminum alloy welded joints into different zones by the microstructure and mechanical properties, the location of the micro-hardness test and the nanoindentation test are generally based on empirical judgment. Due to the limited quantity of selected points, the hardness-based partitioning method has a limitation in accurately determining the partition boundary in the welded joint. Another method for partition aluminum alloy welded joint is based on the metallographic analysis. Microscopic observation is the main method to study the microstructure of materials. Microscopic observation can provide lots of material information, including the morphology of the phases present in the material, the grain size, the distribution of these phases and the non-metallic inclusions in the structure. The microstructure of various materials produced by different processing techniques can be determined, and the properties of the materials can be distinguished. Therefore, many studies have used metallographic microscopy to distinguish different regions for welded joints. Hector [14] and Lemmen [15] used metallographic analysis to partition the friction stir welded joints of aluminum alloys. Based on the experimental results, the different mechanical properties of aluminum alloy welded joints in different regions are evaluated. In addition, Liu [16] used metallographic analysis technology to characterized the welded joint of 2219-T6 aluminum alloy. Combined with tensile test, the effect of the direction of friction stir welding on the mechanical properties of both sides of welded joints is studied.

These abovementioned methods face the challenges of identifying the boundaries between different zones and the evolution principle of material properties, i.e., modulus and strength is difficult to be identified in different zones. The boundary position is critical to the material performance as the mechanical/structural discontinuity at the boundary leads to stress concentration that is dangerous for the structure. Rao [17] showed that the existence of a weakened area is an important factor for the failure of welded joints. Therefore, it is important to accurately and efficiently determine the extent of the welded joints. Therefore, a detailed mapping of mechanical properties in the welded joint is valuable to the fine analysis of the mechanical performance of the whole welded joints.

In this paper, standard tensile experiments of the AA2219 welded joint are conducted and the functional relationship that can express the mechanical properties of any position on the welded joint is proposed based on a fine partitioning scheme. A theory of the evolution of elastoplastic behavior of the AA2219 is proposed as the fundaments of further engineering calculation. The partitioning method presented in this article has two main advantages over the classical methods. One is that the mechanical properties of the welded joint can be obtained at the same time as the partition and reduce the cost of metallographic test. In addition, the distribution of mechanical properties in each region can also be obtained. The other is that the partition boundary can be determined accurately, which avoids the possible error caused by human eye observation. At last, experimental characterizations including scanning electron microscopy (SEM), metallographic microscopy, nanoindentation, and atomic force microscopy (AFM) are used to validate this partitioning scheme.

2. Materials and Methods

2.1. Welded Joints

The BM under investigation is an 8-mm-thick AA2219 plate shown in Figure 1. The chemical compositions of the BM are listed in Table 1. Butt weld is made along the longitudinal direction (perpendicular to the rolling direction) of the welding samples by using an FSW machine. The welding tool consisted of a smooth concave shoulder and a conical right-hand screwed pin. The rotation speed and the welding speed are 600 rpm and 200 mm/min, respectively.

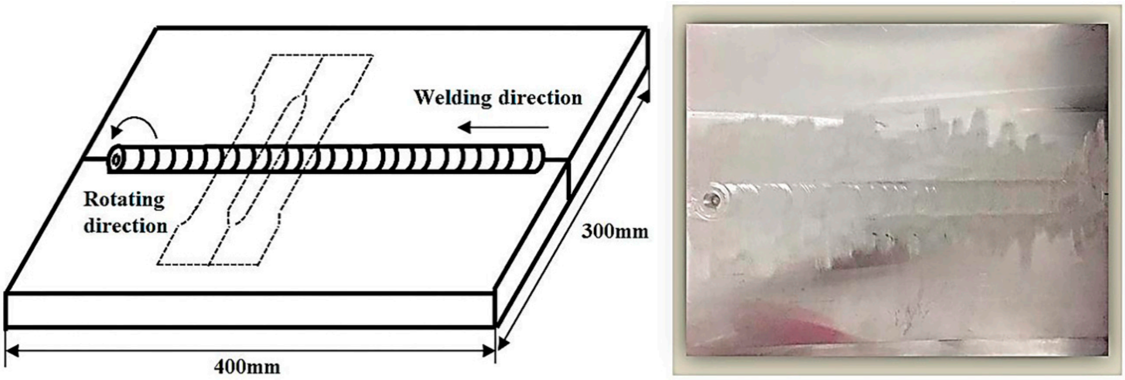

Figure 1. Friction stir-welded plate.

Table 1. Chemical composition of 2219 aluminum alloy.

Element	Si	Fe	Cu	Mn	Zr	Al
Mass Fraction%	0.2	0.3	5.8–6.8	0.3	0.18	Bal

2.2. Tensile Test

After welding, the joints are all cross-sectioned perpendicular to the welding direction for tensile tests. The tensile specimens are conducted strictly following tensile test standards, and the dimensions of the specimen are shown in Figure 2. It should be noted that the tensile specimen retains the weld residual height. In order to measure the mechanical properties of different regions of the welded joints accurately, both electrical (electrical gauge) and optical (digital imaging correlation) measurements are used to obtain the overall variation of the strain history in the entire welding-related area, and the real-time stress data are read by a tensile tester (Material Test System-MTS, Eden Prairie, MN, USA). The equipment can provide a maximum load of 100 kN. The specimen is loaded by displacement and the loading speed is set as 0.5 mm/min.

Strain gauges are arranged at the positions of the WZ and the HAZ of the tensile specimen, measurement point 1 is located on the middle of one edge of the test piece, and measurement point 4 is on the other edge on the same cross section of the WZ with measurement point 1. Measurement points 2, 3, 5, and 6 are in the HAZ and are equidistant from the center of the weld. Figure 3 is a schematic view showing the positions of these electrical measurement points of the tensile specimen.

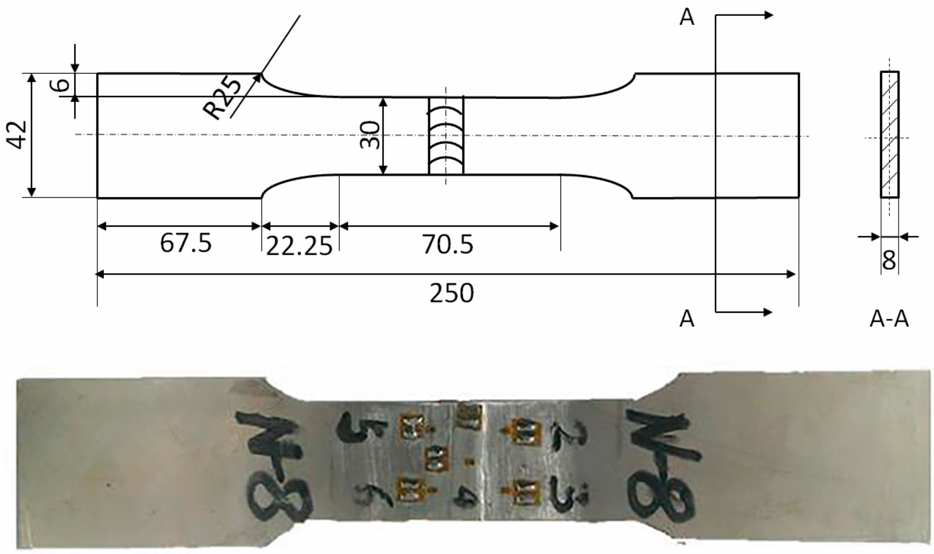

Figure 2. Stretched sample shape size. (Unit: mm).

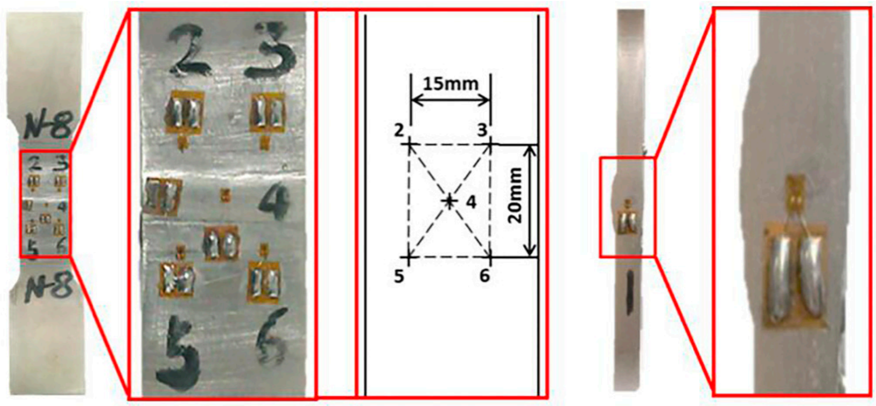

Figure 3. Schematic diagram of the position of the electrical measurement point of the tensile specimen.

2.3. *Digital Imaging Correlation*

In recent years, with the improvement of digital imaging technology, the DIC method has been rapidly developed [18]. This method can accurately obtain the displacement field of the surface of the part and combine the computer analysis techniques to obtain the surface strain field. Compared to traditional strain gauge [19], the measurement range of DIC is not affected by the deformation size, and the measurement points are not limited by the number of strain gauge. The effective measurement range of the conventional strain gauge used in this experiment is 4000 micro-strain, which is limited for capturing the whole strain history of the tensile test. Many researchers worked on the DIC method to obtain the local mechanical properties of welded joint. Reynolds and Duvall [20] first applied the DIC technique to determine the constitutive relations of friction stir-welded joints [21–23] and laser-welded joints [24,25].

DIC method is applied in this work to obtain the detailed strain information during mechanical testing, the positions selected for DIC characterization are shown in Figure 4a. Because the aim of this paper is to present a method to partition the welded joints, the iso-stress condition is assumed in this work, which ensures the material properties of all cross-sections of aluminum alloy welded joints are consistent during the test [26]. In order to get the variation trend of strain field, 9 points are selected along the length direction of the specimen to obtain the strain history during the tensile test for the later partitioning purpose. It is necessary to point out that optical measurement point 5 and electrical measurement point 1 are in symmetrical positions on the two sides of the specimen, which can be used for method validation of optical measurements. Figure 4b shows the test apparatus (including the loading machine and the imaging system).

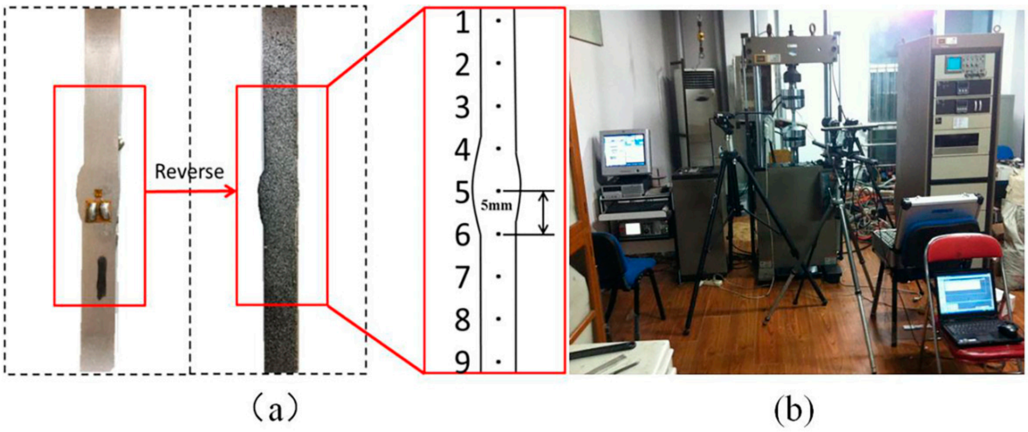

Figure 4. Positions selected for DIC and Test apparatus: (**a**) Positions selected for DIC, (**b**) Test apparatus including the loading machine and the imaging system.

2.4. Metallographic Microscopy

In this study, the test is conducted to determine the microstructure the aluminum alloy welded joints on the metallographic microscopy (MEF-4, Keyence, Osaka, Japan) as a proof for the partitioning strategy proposed in this paper. This device can be applied to the use of reflective metal materials to determine their histological morphology and microstructure. The metallographic microscopy test intercepts the sample along the cross-section of the sample (rolling direction), then etches the polished sample with mixed acid (1.0%HF + 1.5%HCl + 2.5%HNO_3 + 95.0%H_2O) for 30 s, and observes the microstructure of the base metal and FSW welded joint. The size of the sample is 80 mm × 10 mm × 4 mm (length × width × height), and the measuring points at each position are three.

2.5. SEM (EDS)

SEM imaging is conducted on the field emission scanning electron microscopy (SUPRA55, Germany). This device could provide magnification from ×12 to ×500,000, and it can be applied to the use of reflective metal materials to determine their microstructure, and elements of specimens can be analyzed quantitatively and qualitatively by energy dispersive spectroscopy (EDS) module. The SEM test intercepts the sample along the cross-section of the sample (rolling direction), similar to the metallographic microscopy test, then etches the polished sample with mixed acid (1.0%HF + 1.5%HCl + 2.5%HNO_3 + 95.0%H_2O) 90 s, then observes the microstructure of the FSW welded joint by the field emission scanning electron microscopy. The size of the sample is 50 mm × 10 mm × 5 mm (length × width × height), and the measuring points at each position are three.

2.6. Nano-Indentation

Nanoindentation test is an effective method to identify the local property of materials in the welded joint. In this study, the nanoindentation test is conducted on the nano-indentation testing machine (Hysitron TI-950, USA) to validate the partitioning method proposed in this paper. The instrument has a 500 nm resolution microscopy in a top view for precise positioning of test points. The indentation test can record the load-displacement data during the process and fit the calculated elastic modulus, hardness equivalent. In order to determine the difference in local mechanical properties of welded joints, a range of 20 mm from the center of the weld is selected for measurement in this experiment. The size of the sample is 50 mm × 10 mm × 5 mm (length × width × height), and the measuring points at each position are three.

at each position are three.

2.7. Atomic Force Microscopy

In order to validate partition results more comprehensively, atomic force microscopy (AFM) test is conducted (Bruker Dimension Icon, Germany) to provide the surface morphology of materials at the nanoscale to show the variation of surface morphology between different zones. In the AFM test, the observation scope (5 μm × 5 μm) is taken. The size of the sample is 80 mm × 10 mm × 4 mm (length × width × height), and the measuring points at each position are three.

3. Partitioning Strategy

3.1. Tensile Behavior of Welded Joints

Based on the real-time loading output and the incompressibility of plastic deformation, the true stress during the tensile process of each measurement point can be calculated. A comparison between the optical measurement results and the electrical measurement results at the same cross-section is carried out to validate the reliability of DIC method for the welded joints. The results showed that the electrical measurement and the optical measurement results are in good agreement, as shown in Figure 5a. Compared to strain gauges, the DIC method can provide the displacement field and strain field on the sample, as shown in Figure 5b, enabling the stiffness mapping of the welded joints based on the assumption that the various weld regions are arranged in series and the cross-section at any location in the specimen is homogeneous [26]. In Figure 5b, "*V*[mm]" is the displacement in the direction of loading, "eyy [1] Lagrange" is the strain in the direction of loading.

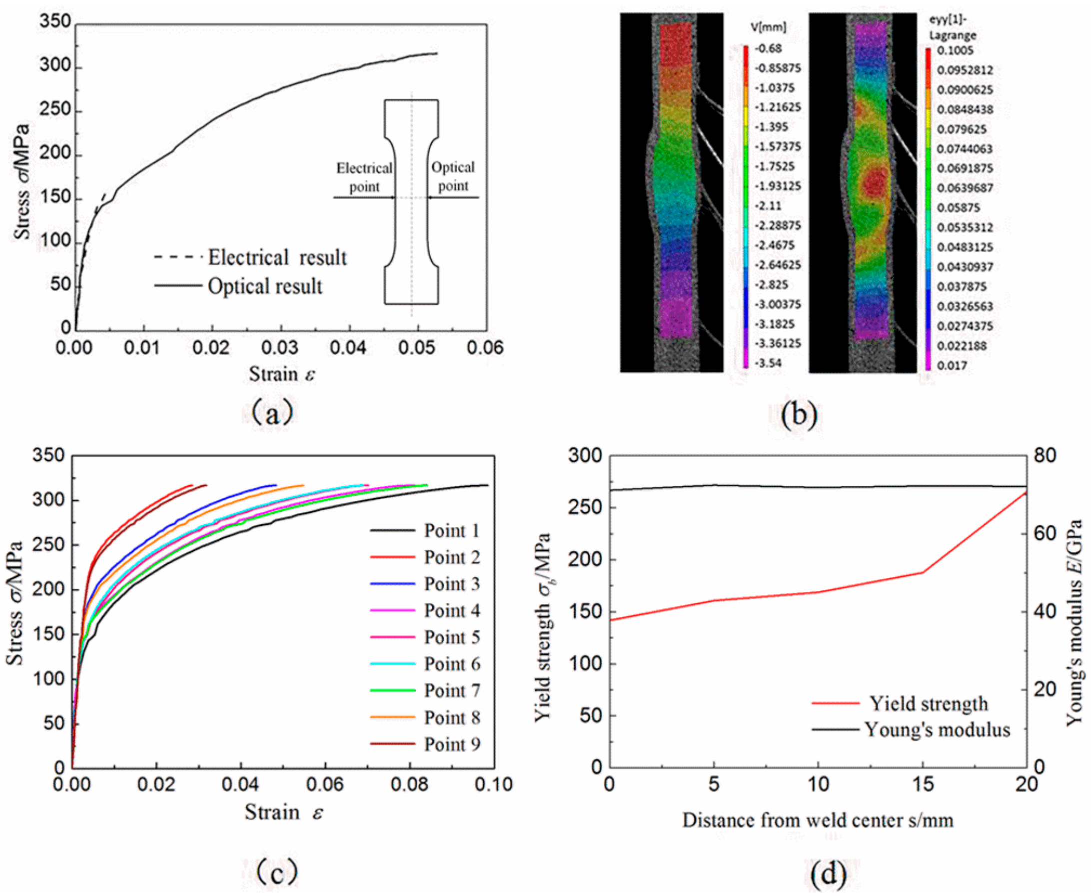

Figure 5. Tensile test results of 2219 aluminum alloy welded joints: (**a**) Stress-strain comparison curve of electrical photometry at the same cross-section, (**b**) optical results diagram, (**c**) photometric stress-strain curve, (**d**) the yield strength curve and the modulus of elasticity curve.

The stress-strain curves at each measurement point are provided in Figure 5c and the corresponding Young's modulus and yield strength are shown in Figure 5d. Here, as the data results are symmetric along the weld center, only the results of one side of the weld center are given in Figure 5d. The Young's modulus shows no variation with respect to the distance from the center line (near 70 GPa), however the yield strength increases with the value of distance (from 150 to 260 MPa), indicating that the plastic properties of a material is the major changing characteristic due to the heat treatment in the welding operation.

3.2. Plasticity Model in Welding Joints

A new partitioning strategy is proposed in this section and the flowchart of this strategy is shown in Figure 6.

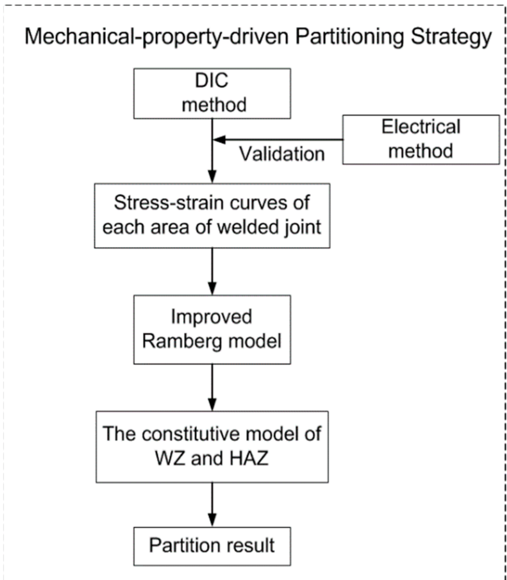

Figure 6. Flowchart of the partitioning strategy.

For elastoplastic materials, a stress-strain constitutive relation proposed by Ramberg et al. [27] in the form of a power function is often used, which is shown as Equation (1); the two parameters H and n are strength coefficient and strain hardening exponent, respectively.

$$\varepsilon = \frac{\sigma}{E} + \left(\frac{\sigma}{H}\right)^{\frac{1}{n}} \quad (1)$$

In this equation, the strain is expressed as a sum of elastic strain and plastic strain. In addition, σ is stress, ε is strain, E is the Young's modulus, and H and n are the parameters to be determined by the least-squares method. If we assume the value of H and n are constants for the whole welding joint, these two parameters can be directly obtained by fitting the experiment results and should be similar for different measurement points in the welded joint. However, after parameters fitting, it can be found that these parameters vary with respect to the distance to the center line, which is shown in Table 2, proving that a simple constant definition of the parameters H and n cannot accurately describe the evolution of plasticity in the welding joint.

Table 2. Fitting results of H and n values.

Number	1	2	3	4	5	6	7	8	9
H	457.899	524.807	583.647	579.322	553.554	609.958	611.871	531.496	458.543
n	0.104	0.163	0.226	0.213	0.224	0.234	0.221	0.173	0.108

Herein, a new mechanical-property-driven partitioning strategy is proposed to describe the uneven distribution of materials due to the welding operation. Based on the symmetry of welding joints, only the data on one side of the welded joint are selected for later analysis, and each data point is 1 mm apart from the next point, as shown in Figure 7a. A constitutive relationship includes the WZ and the HAZ is proposed based on the evolution of parameters (n and H) in the welding joints. The parameters are summarized as functions ($H = f(\mathrm{s})$, $1/n = g(s)$) of the distance from the center line of welding (s), and the constitutive relationship in Equation (1) can be revised as Equation (2). For AA2219, these functions can be simplified as polynomial functions, as shown in Equations (3) and (4).

$$\varepsilon = \frac{\sigma}{E} + \left(\frac{\sigma}{f(s)}\right)^{g(s)} \tag{2}$$

For WZ:

$$\begin{cases} f(s) = as^2 + bs + c \\ g(s) = d \end{cases} \tag{3}$$

For HAZ:

$$\begin{cases} f(s) = as + b \\ g(s) = cs^2 - ds + e \end{cases} \tag{4}$$

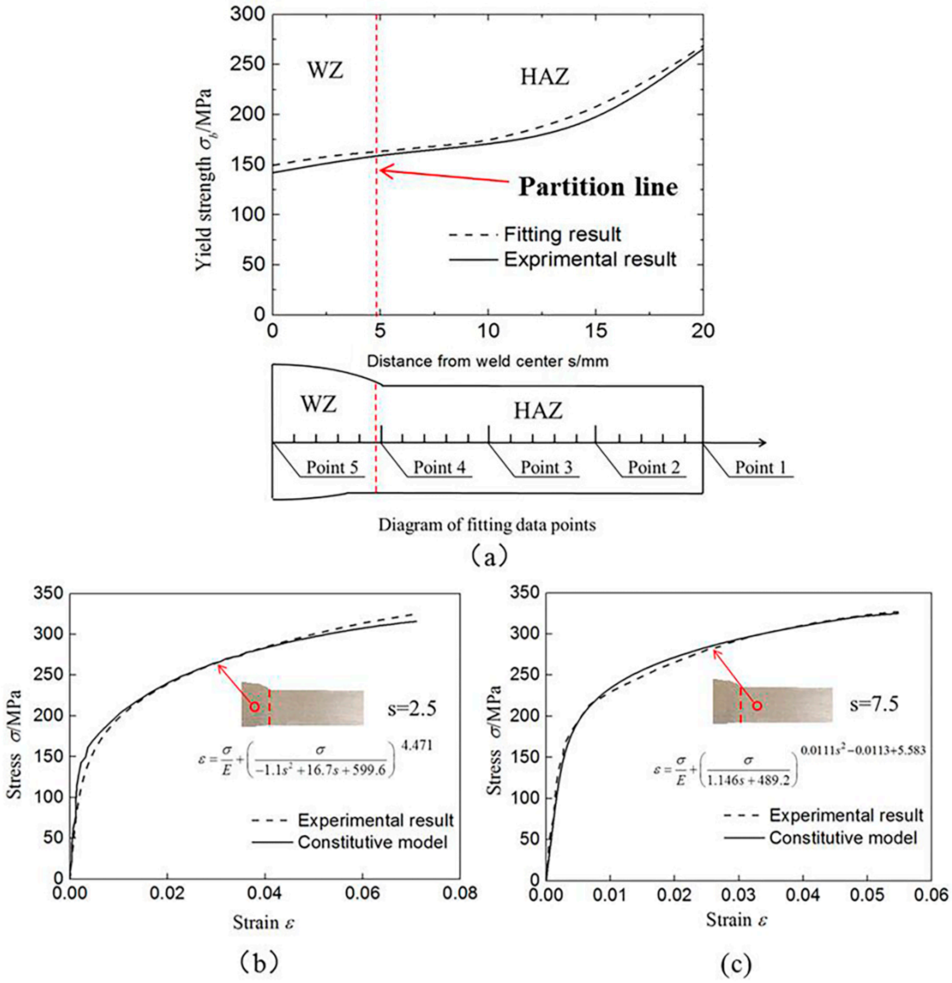

Figure 7. Comparisons of test results and mathematical models: (**a**) Yield strength curve for the whole area, (**b**) stress-strain curve in WZ, (**c**) stress-strain curve in heat affected zone (HAZ).

According to the abovementioned rules, the welded joints can be partitioned based on the Equations (3) and (4). In this study, all the parameters can be determined by the data fitting. At last, Equations (5) and (6) are obtained for WZ and HAZ in AA2219 welding joints, respectively. Therefore, the intersection of the two curves in Equations (5) and (6) can be determined as the boundary between WZ and HAZ. For this friction stirred welding joint, the position of the boundary line is determined to be 4.815 mm from the center of the weld, as shown in Figure 7.

For WZ:

$$\begin{cases} f(s) = -1.1s^2 + 16.7s + 599.6 \\ g(s) = 4.471 \end{cases} \tag{5}$$

For HAZ:

$$\begin{cases} f(s) = 1.146s + 489.2 \\ g(s) = 0.0111s^2 - 0.0113s + 5.583 \end{cases} \tag{6}$$

In order to validate this partitioning result, two random points are selected in the WZ and the HAZ to verify the Equations (5) and (6), respectively. The distance from the weld center is 2.5 mm and 7.5 mm. The comparison between the mathematical model and the test results is shown in Figure 7b,c. The comparison between the mathematical model of the weld zone and the heat affected zone and the test results is good, and the maximum error is less than 8%, which indicated that Equations (5) and (6) can effectively describe the mechanical properties distribution of different joints in the AA2219 welded joints after friction stir welding.

4. Validation of the Partitioning Strategy

4.1. Metallographic Characteristics

Figure 8 is the microstructure of 2219 aluminum alloy welded joint given by metallographic microscopy, which shows a distinct difference from the WZ to the BM. The microstructure variation from the WZ to the HAZ is more drastic than the HAZ to the BM. It can be seen that the BM has an obvious trace of rolling direction and the shape of the grains of BM is stretched towards the rolling direction. The weld nugget area is affected by the welding heat cycle and agitation, and the morphology changes significantly. During the FSW process, a large amount of heat is generated between the stirring needle and the workpiece and the shoulder of the stirring head to the workpiece, so that the surrounding metal is plasticized and plastic flow enough. The density of the dislocations increases with the stirring force, and when the stored energy is increased to a certain extent. The density of the dislocations increases with the stirring force. When the stored energy is increased to a certain extent, the crystal nucleus begins to form continuously in the metal, and the structure undergoes dynamic re-crystallization. The lamella structure of the original base material is transformed into an equiaxed recrystallized structure, and the crystal grains are uniform, and the average size is much smaller than the grain size of BM (Figure 8a). The TMAZ is a long narrow area, which is located at the boundary of WZ and HAZ in this work. This area is affected by the mixing needle and the shoulder and is subjected to a higher temperature welding thermal cycle, and the grain has a large bending deformation. As shown in Figure 8b, the grain size is the smallest area in the welded joint. The microstructure of the HAZ is shown in Figure 8c. The HAZ is not directly subjected to agitation during the welding process, is only subjected to thermal cycling during the welding process, and the grain sizes are not uniform, so a part of the grains retain the characteristics of BM and a part of the grains has a smaller size. It is necessary to point out that the separation line between HAZ and BM zones have been obtained by visual inspection. According to the difference of the metallographic characteristics of each area of the welded joint, the partition of the welded joint is determined. The proposed method in this paper is consistent with the observation result.

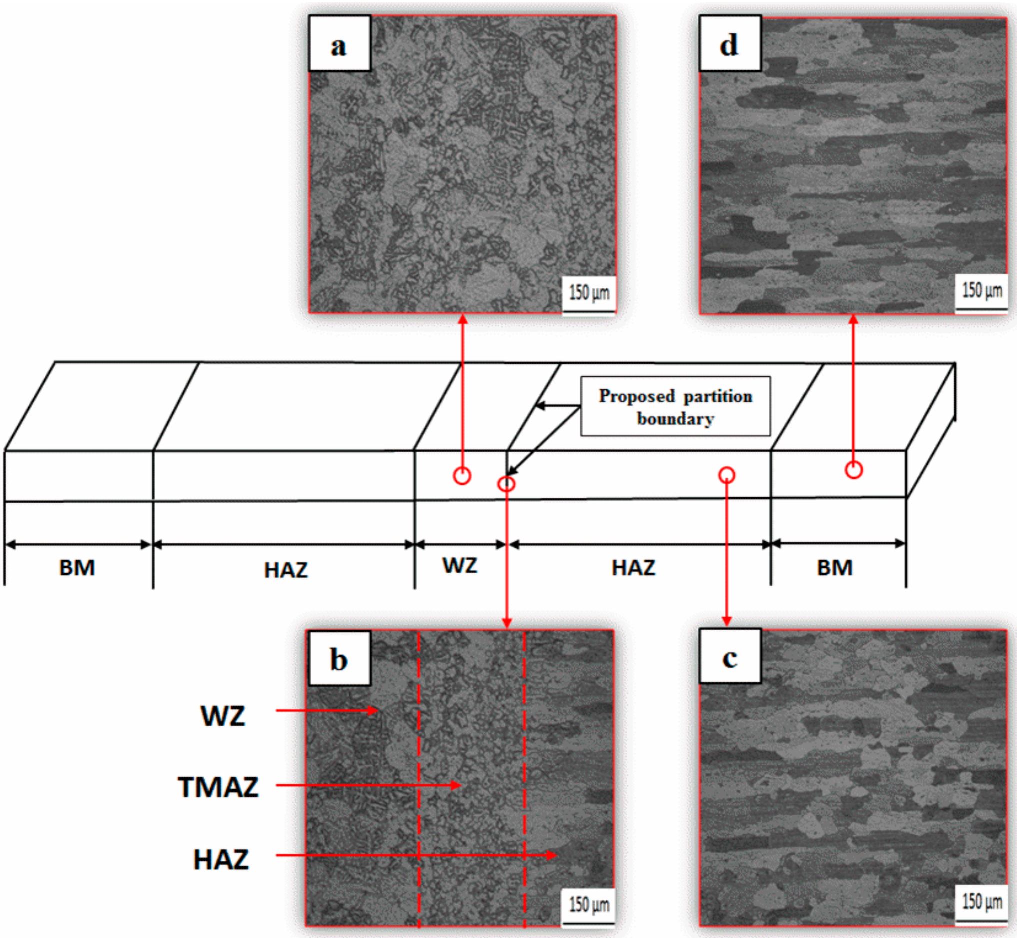

Figure 8. The microstructure of 2219 aluminum alloy welded joint given by metallographic microscopy. (**a**) weld zone (WZ), (**b**) thermo-mechanically affected zone (TMAZ), (**c**) HAZ, (**d**) base metal (BM).

4.2. SEM Morphological Characteristics

The precipitated phase of the joint is affected by the welding heating cycle and agitation, and there are significant differences in the distribution patterns of the joints. Figure 9 shows scanning electron micrographs of FSW of 2219-T87 aluminum alloy. The 2219 aluminum alloy is based on α(Al) and contains many small particles. The white particles are analyzed by electron spectroscopy (EDS analysis). The results are shown in Table 3, where SD represents standard deviation value. It shows that the components of the α phase in three different parts of WZ, TMAZ, and HAZ are basically the same, but the precipitated phase is quite different. The partition result determined by the proposed method agrees well with the SEM morphological observation.

Table 3. EDS results.

Position	Al (SD%)	Cu (SD%)	Fe (SD%)	Mn (SD%)
α phase of WZ	97.17 (0.1)	2.83 (1.6)	-	-
Precipitated phase of WZ	59.22 (0.6)	40.78 (0.7)	-	-
α phase of TMAZ	97.26 (0.1)	2.74 (2.8)	-	-
Precipitated phase of TMAZ	60.49 (0.5)	32.27 (0.8)	5.8 (1.2)	1.44 (2.2)
α phase of HAZ	93.07 (0.1)	6.93 (1.7)	-	-
Precipitated phase of HAZ	46.98 (0.7)	43.43 (0.6)	8.1 (2.0)	1.49 (3.1)

SEM results of different magnification of the WZ are shown in Figure 9a,d. In the welding process, WZ maintains a high temperature and has enough time to form precipitation phase in the grain, so it can be seen that there are precipitation phases in the grain and at the grain boundary. As a result of recrystallization, grains of uniform size are formed, and the radius of the grain size in WZ is about 25 µm.

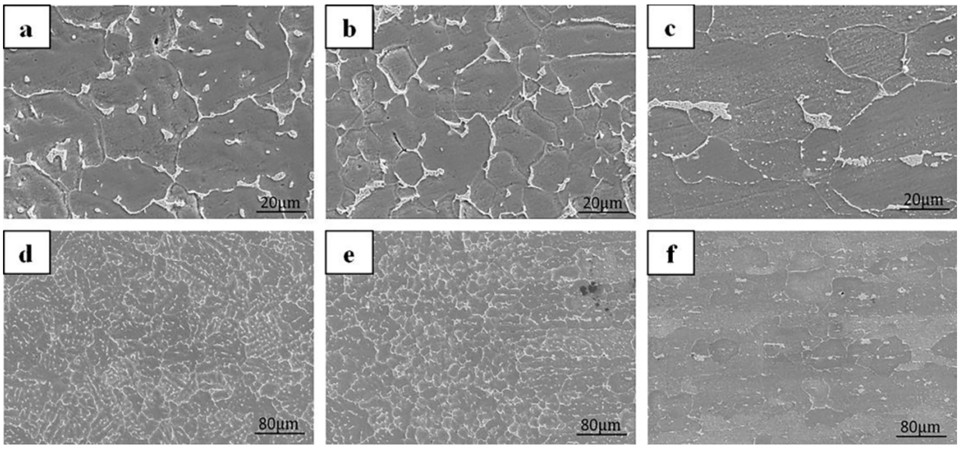

Figure 9. The microstructure of 2219 aluminum alloy welded joint measured by SEM. (**a**) WZ magnified 2000 times, (**b**) TMAZ magnified 2000 times, (**c**) HAZ magnified 2000 times, (**d**) WZ magnified 500 times, (**e**) TMAZ magnified 500 times, (**f**) HAZ magnified 500 times.

The results of different magnification of the TMAZ are shown in Figure 9b,e. The temperature in the affected area is not as high as the weld nugget zone, but the action time is longer. After stirring and welding thermal cycle, the local dynamic recrystallization of grains occurs, and some precipitated phase is located at the boundary of the grains.

In the HAZ, the heating near the heat source is fast, the peak temperature is high, and the cooling speed is higher. Therefore, the microstructure in the HAZ also has a large difference. Due to the high peak temperature, in the HAZ near the WZ, the grain grows significantly; much larger than the size of the grain in the base metal, and the shape is equiaxed, as shown in Figure 9c,f.

4.3. Nano-Mechanical Characteristics

In this study, nano-indentation is also conducted to validate the partitioning method proposed in this paper. The test result is shown in Figure 10, the hardness of WZ increases with the distance from the welding center, and there is a sudden change at the junction with HAZ. The maximum hardness is found at the junction of WZ and HAZ. It has been reported by Cavaliere [28] and Yazdipour [13] that the grain size is smaller at the junction of WZ and HAZ, resulting in a higher hardness. This is because the material flow at the junction is more serious compared to the other areas, which produces finer microstructures at a higher rotation speed. Since then, the boundary of the WZ and HAZ lies between 4 mm and 5 mm from the weld center line, which agrees well with prediction results by the proposed method.

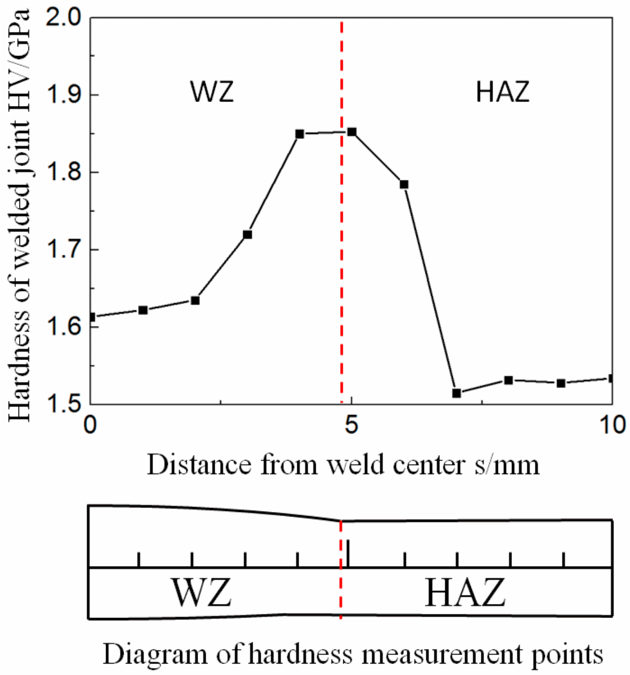

Figure 10. Nanoindentation test hardness of the welded joint (red line denotes the boundary obtained by the partitioning method proposed in this paper).

4.4. Surface Characteristics

AFM test is conducted as an assistant proof of the partition result as it can give the variation of surface morphology between different areas. Within 10 mm from the centerline of the welding, three measurement points are selected every 1 mm. The surface roughness (*R*a: Arithmetic mean roughness) of the material in different areas are calculated and shown in Figure 11 (5 µm × 5 µm). The results show that the average roughness of WZ is obviously higher than that of HAZ, and the boundary of WZ and HAZ has the lowest roughness value.

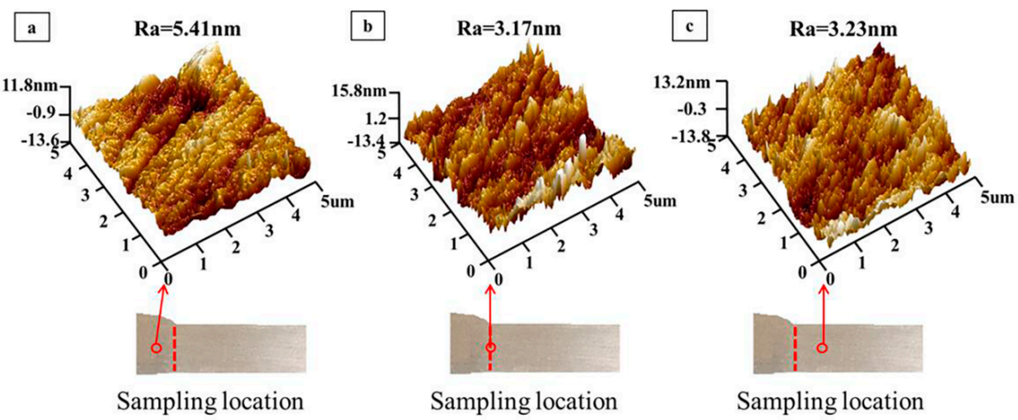

Figure 11. Surface morphology results of the welded joint. (**a**) Surface morphology of WZ, (**b**) surface morphology of partition line, (**c**) surface morphology of HAZ.

5. Conclusions

Due to the development of the DIC method, the research on welded joints is no longer limited to a specific mechanical property of each area, but can obtain the mechanical property of every point on the whole welded joint. In this paper, based on the standard tensile test and the elastoplastic mechanical model, an elastoplastic constitutive model is established to express the mechanical properties of any point of AA2219 welded joint. According to the elastoplastic constitutive model, the partition scheme of the welded joint of AA2219 is given, and the boundary between the WZ and the HAZ of the AA2219 welded joint of friction stir welding is determined. Finally, a series of verification tests are carried out. The results show that the partitioning result of the strategy proposed in this paper is consistent with partitioning result of the classical method. The proposed method can not only accurately determine the partition boundary, but also obtain the mechanical properties of the welded joint at the same time effectively.

Author Contributions: Conceptualization, G.C. and M.R.; validation, Y.Z.; data curation, G.C.; writing—original draft preparation, G.C. and T.L.; writing—review and editing, G.C. and T.L.; project administration, W.P.; funding acquisition, M.R. All authors have read and agreed to the published version of the manuscript.

Funding: This research was supported by the National Basic Research Program of China (2014CB046506, 2014CB049000), the National Natural Science Foundation of China (11372058, 11802053), and the Start-up funding from DUT (DUT18RC(3)031).

Conflicts of Interest: The authors declare no conflict of interest.

References

1. Arora, K.S.; Pandey, S.; Schaper, M.; Kumar, R. Effect of process parameters on friction stir welding of aluminum alloy 2219-T87. *Int. J. Adv. Manuf. Technol.* **2010**, *50*, 941–952. [CrossRef]
2. Elangovan, K.; Balasubramanian, V. Influences of pin profile and rotational speed of the tool on the formation of friction stir processing zone in AA2219 aluminium alloy. *Mater. Sci. Eng. A* **2007**, *459*, 7–18. [CrossRef]
3. Xu, W.; Liu, J.; Luan, G.; Dong, C. Temperature evolution, microstructure and mechanical properties of friction stir welded thick 2219-O aluminum alloy joints. *Mater. Des.* **2009**, *30*, 1886–1893. [CrossRef]
4. Al-Fadhalah, K.J.; Almazrouee, A.I.; Aloraier, A.S. Microstructure and mechanical properties of multi-pass friction stir processed aluminum alloy 6063. *Mater. Des.* **2014**, *53*, 550–560. [CrossRef]
5. Ma, Z.Y.; Mishra, R.S.; Mahoney, M.W.; Grimes, R. High strain rate superplasticity in friction stir processed Al–Mg–Zr alloy. *Mater. Sci. Eng. A* **2003**, *351*, 148–153. [CrossRef]
6. Agarwal, S.; Briant, C.L.; Hector, L.G.; Chen, Y.-L. Friction stir processed AA5182-O and AA6111-T4 aluminum alloys. Part 1: Electron backscattered diffraction analysis. *J. Mater. Eng. Perform.* **2007**, *16*, 391–403. [CrossRef]
7. Cao, G.; Huang, C.; Li, T.; Zhang, Y.; Ren, M. Mechanical Characterization of 2219 Aluminum Alloy Welded Joints Under Bi-axial Loading. *Int. J. Appl. Mech.* **2019**. [CrossRef]
8. Boccarusso, L.; Astarita, A.; Carlone, P.; Scherillo, F.; Rubino, F.; Squillace, A. Dissimilar friction stir lap welding of AA6082-MgAZ31: Force analysis and microstructure evolution. *J. Manuf. Process.* **2019**, *44*, 376–388. [CrossRef]
9. Mehta, K.P.; Carlone, P.; Astarita, A.; Scherillo, F.; Rubino, F.; Vora, P. Conventional and cooling assisted friction stir welding of AA6061 and AZ31B alloys. *Mater. Sci. Eng. A* **2019**, *759*, 252–261. [CrossRef]
10. Viscusi, A.; Astarita, A.; Prisco, U. Mechanical properties optimization of friction stir welded lap joints in aluminium alloy. *Adv. Mater. Sci. Eng.* **2019**. [CrossRef]
11. He, J.; Ling, Z.; Li, H. Effect of tool rotational speed on residual stress, microstructure, and tensile properties of friction stir welded 6061-T6 aluminum alloy thick plate. *Int. J. Adv. Manuf. Technol.* **2015**, *84*, 1953–1961. [CrossRef]
12. Rojek, J.; Hyrcza-Michalska, M.; Bokota, A.; Piekarska, W. Determination of mechanical properties of the weld zone in tailor-welded blanks. *Arch. Civ. Mech. Eng.* **2012**, *12*, 156–162. [CrossRef]
13. Yazdipour, A.; Heidarzadeh, A. Effect of friction stir welding on microstructure and mechanical properties of dissimilar Al 5083-H321 and 316L stainless steel alloy joints. *J. Alloys Compd.* **2016**, *680*, 595–603. [CrossRef]
14. Hector, L.G.; Chen, Y.L.; Agarwal, S.; Briant, C.L. Friction stir processed AA5182-O and AA6111-T4 aluminum alloys. Part 2: Tensile properties and strain field evolution. *J. Mater. Eng. Perform.* **2007**, *16*, 404–417. [CrossRef]
15. Lemmen, H.J.K.; Alderliesten, R.C.; Pieters, R.R.G.M.; Benedictus, R.; Pineault, J.A. Yield strength and residual stress measurements on friction-stir-welded aluminum alloys. *J. Aircr.* **2010**, *47*, 1570–1583. [CrossRef]
16. Liu, H.; Zhang, H.; Pan, Q.; Yu, L. Effect of friction stir welding parameters on microstructural characteristics and mechanical properties of 2219-T6 aluminum alloy joints. *Int. J. Mater. Form.* **2011**, *5*, 235–241. [CrossRef]

17. Rao, D.; Huber, K.; Heerens, J.; dos Santos, J.F.; Huber, N. Asymmetric mechanical properties and tensile behaviour prediction of aluminium alloy 5083 friction stir welding joints. *Mater. Sci. Eng. A* **2013**, *565*, 44–50. [CrossRef]
18. Hwang, S.F.; Shen, M.C.; Hsu, B.B. Strain measurement of polymer materials by digital image correlation combined with finite-element analysis. *J. Mech. Sci. Technol.* **2015**, *29*, 4189–4195. [CrossRef]
19. Parida, B.; Vishwakarma, S.D.; Pal, S. Design and development of fixture and force measuring system for friction stir welding process using strain gauges. *J. Mech. Sci. Technol.* **2015**, *29*, 739–749. [CrossRef]
20. Reynolds, A.P.; Duvall, F. Digital image correlation for determination of weld and base metal constitutive behavior. *Weld. J.* **1999**, *78*, 55–60.
21. Brown, R.; Tang, W.; Reynolds, A.P. Multi-pass friction stir welding in alloy 7050-T7451: Effects on weld response variables and on weld properties. *Mater. Sci. Eng. A* **2009**, *513–514*, 115–121. [CrossRef]
22. Genevois, C.; Deschamps, A.; Vacher, P. Comparative study on local and global mechanical properties of 2024 T351, 2024 T6 and 5251 O friction stir welds. *Mater. Sci. Eng. A* **2006**, *415*, 162–170. [CrossRef]
23. Hatamleh, O. Effects of peening on mechanical properties in friction stir welded 2195 aluminum alloy joints. *Mater. Sci. Eng. A* **2008**, *492*, 168–176. [CrossRef]
24. Boyce, B.L.; Reu, P.L.; Robino, C.V. The constitutive behavior of laser welds in 304L stainless steel determined by digital image correlation. *Metall. Mater. Trans. A* **2006**, *37*, 81–92. [CrossRef]
25. Scintilla, L.D.; Tricarico, L.; Brandizzi, M.; Satriano, A.A. Nd:YAG laser weldability and mechanical properties of AZ31 magnesium alloy butt joints. *J. Mater. Process. Technol.* **2010**, *210*, 2206–2214. [CrossRef]
26. Lockwood, W.D.; Reynolds, A.P. Simulation of the global response of a friction stir weld using local constitutive behavior. *Mater. Sci. Eng. A* **2003**, *339*, 35–42. [CrossRef]
27. Ramberg, W.; Osgood, W.R. *Description of Stress-Strain Curves by Three Parameters*; Technical Report; Archive & Image Library: Chicago, IL, USA, 1943.
28. Cavaliere, P.; Nobile, R.; Panella, F.W.; Squillace, A. Mechanical and microstructural behaviour of 2024–7075 aluminium alloy sheets joined by friction stir welding. *Int. J. Mach. Tools Manuf.* **2006**, *46*, 588–594. [CrossRef]